



RESEARCH ARTICLE

10.1029/2018JC014284

The Competing Effects of Breaking Waves on Surfzone Heat Fluxes: *Albedo Versus Wave Heating*

Key Points:

- Surfzone breaking waves heat via dissipation; foam increases albedo, reducing solar radiation
- Over a year, the albedo-induced solar heating reduction was most significant
- The net effect depends on incident wave height, latitude, seasons, beach slope, and cloudiness

Correspondence to:

G. Sinnett,
gsinnett@ucsd.edu

Citation:

Sinnett, G., & Feddersen, F. (2018). The competing effects of breaking waves on surfzone heat fluxes: *Albedo versus wave heating*. *Journal of Geophysical Research: Oceans*, 123. <https://doi.org/10.1029/2018JC014284>

Received 18 JUN 2018

Accepted 13 SEP 2018

Accepted article online 17 SEP 2018

Gregory Sinnett¹ and Falk Feddersen¹¹Scripps Institution of Oceanography, University of California, San Diego, La Jolla, CA, USA

Abstract Depth-limited wave breaking modifies the heat flux in the surfzone relative to the inner-shelf (where waves are not breaking). Surfzone wave breaking generates heat through viscous dissipation (wave heating), but also increases surface foam coverage and albedo, thereby reducing solar heating, that is, cooling relative to the inner-shelf. These two competing breaking wave effects are quantified with a yearlong experiment at the Scripps Institution of Oceanography Pier. Cross-shore averaged surfzone albedo estimates were more than three times higher than inner-shelf albedo, reducing the yearly averaged surfzone water-entering shortwave radiation by 41 W/m² relative to the inner-shelf. Surfzone breaking wave dissipation added an additional yearly averaged 28 W/m² relative to the inner-shelf. The albedo-induced solar heating reduction in spring, summer, and fall was usually greater than the wave heating. However, in winter, large waves and relatively weak shortwave solar radiation (due to both lower top of the atmosphere solar radiation and clouds) resulted in a nearly equal number of days of breaking wave-induced heating or cooling. These two heat flux terms are coupled via wave breaking dissipation. Averaged over the surfzone, the albedo-induced solar radiation reduction is linearly related to the downwelling solar radiation and is independent of wave height. Consequently, the albedo-induced cooling to wave heating ratio is a function of breaking wave height to the $-3/2$ power, allowing evaluation of the relative importance of these terms in other geographic regions.

Plain Language Summary Temperature variation in nearshore waters affects the local ecology, and is also used to study important physical processes. Wave breaking contributes to surfzone temperature variation in two ways. First, breaking waves dissipate their energy in the surfzone creating friction (heat) and foam. Surfzone foam reflects sunlight reducing solar warming of the surfzone, thus leading to cooling relative to no wave breaking. These two competing wave effects (addition of frictional heating and reduction in solar heating) are quantified with a yearlong experiment at the Scripps Institution of Oceanography pier (La Jolla, CA). On average, frictional wave heating added 28 W to each square meter of surfzone. At the same time, surface foam reduced the solar heating in each square meter of surfzone by 41 W on average. The relative contribution of these competing effects varied depending on the wave height and the available sunlight, which depended on seasons and clouds. Temperature variation caused by these two effects can be estimated at other locations if the wave height and the amount of sunlight are known.

1. Introduction

The surfzone (region of depth-limited wave breaking) and adjacent offshore shallow inner-shelf (no depth-limited wave breaking) comprise the nearshore; a physically dynamic, economically important, and biologically diverse part of the ocean. Temperature is an important physical attribute here, as temperature variation affects growth rates, recruitment rates, and egg mass production rates of various species (e.g., Broitman et al., 2005; Fischer & Thatje, 2008; Phillips, 2005) as well as pathogen ecology (e.g., Goodwin et al., 2012). Pathogen mortality is related to both temperature (Surbeck, 2009) and exposure to solar shortwave radiation (e.g., Boehm et al., 2002; Sinton et al., 1999, 2002). In the nearshore, temperature can also be a tracer for nutrient delivery (e.g., Omand et al., 2012) or surfzone to inner-shelf water mass exchange (e.g., Hally-Rosendahl et al., 2014).

Consequently, quantitatively understanding physical mechanisms affecting the inner-shelf heat budget has been an active area of recent study. Inner-shelf heat budgets include upwelling (e.g., Fewings & Lentz, 2011; Lentz, 1987), wind stress (e.g., Austin, 1999), eddies (e.g., Wilkin, 2006), internal waves (e.g., Shroyer

©2018. The Authors.

This is an open access article under the terms of the Creative Commons Attribution-NonCommercial-NoDerivs License, which permits use and distribution in any medium, provided the original work is properly cited, the use is non-commercial and no modifications or adaptations are made.

et al., 2010), and the passage of weather systems on time scales of days to weeks (e.g., Austin & Lentz, 1999). Heat transfer between the air-sea interface occurs through radiative solar shortwave heating, net long-wave heat flux, as well as net latent and sensible heat exchange and is often parameterized (e.g., Beardsley et al., 1998; Fairall et al., 1996, 2003) when applied to observational and modeling studies (e.g., Davis et al., 2011; Etter et al., 2004; Lentz, 1987; Wilkin, 2006).

Closer to shore, rip currents (narrow wave-driven ejections from the surfzone) have been associated with strong temperature variation on the inner-shelf (Hally-Rosendahl et al., 2014; Smith & Largier, 1995), interacting with and adjusting the vertical temperature profile and influencing the inner-shelf cross-shore heat flux (Kumar & Feddersen, 2017). Thus, surfzone temperature (relative to the stratified inner-shelf) is an important determining factor for how this transport mechanism is established and evolves. Additionally, the presence of fecal indicator bacteria (FIB) near the Southern California coast varies with temperature (Boehm et al., 2004), and predictive models for pathogen transport in the surfzone include temperature and shortwave radiation (e.g., Boehm, 2003). In addition, solar radiation-induced *Enterococcus* (FIB) mortality contains cross-shore variation, and modeled FIB concentrations and decay rates were best predicted when cross-shore mortality gradients were included (Rippy, Franks, Feddersen, Guza, & Moore, 2013). Thus, cross-shore variation of temperature and solar radiation affects many important biological processes, motivating a more complete understanding of surfzone to inner-shelf temperature and solar radiation differences.

Many aspects of the surfzone heat budget are similar to the inner-shelf heat budget, although surfzone wave breaking modifies terms and creates a new term. The new *wave heating* term is generated by surfzone wave breaking, which through viscous dissipation, generates heat. Also, breaking wave-induced foam increases the surfzone albedo and thereby reduces the water-entering solar shortwave radiation relative to the inner-shelf. Further, surfzone wave breaking affects the sensible (MacMahan et al., 2018) and potentially the latent air-sea fluxes. Here the wave heating and surfzone foam albedo effects are explored.

The wave heating contribution to the surfzone heat budget results from mechanical wave energy being converted to heat (internal energy) through viscous dissipation. Waves outside the surfzone shoal and break in the shallow surfzone, generating turbulent kinetic energy. Some wave energy is reflected from the shoreline, however on shallow sloping beaches (such as in this study) the percentage of reflected wave energy is typically small (<3%; Elgar et al., 1994). Other surfzone processes driven by wave breaking are frictionally balanced with energy pathways still leading to viscous heating. For example, breaking wave-driven along-shore currents are frictionally balanced (Feddersen et al., 1998). Similarly, surfzone wave breaking can suspend sediment or inject bubbles into the water column, yet their fall or rise is also frictionally balanced. Acoustic noise generated by wave breaking does radiate away but noise generation is negligible (6–10 orders of magnitude smaller) relative to breaking wave dissipation (e.g., Kennedy, 1992; Klusek & Lisimenka, 2013). Additional export of mechanical energy from the surfzone (via rip currents or undertow, e.g.) has been estimated to be many orders of magnitude smaller than incident wave energy flux on similar beaches (Sinnott & Feddersen, 2014). Thus, the bulk of the incident wave energy is dissipated in the surfzone through turbulence throughout the water column, and eventually converted to heat. Wave heating heats the surfzone relative to the inner-shelf.

Solar heat flux is a major surfzone heat budget term (Sinnott & Feddersen, 2014), so changes to the albedo, and thus the amount of absorbed solar radiation, are consequential. The surfzone surface is a combination of foam-free and foam-covered areas due to the recent passage of breaking waves (e.g., Frouin et al., 1996). As foam has a higher albedo ($\alpha \approx 0.55$; Whitlock et al., 1982) than foam-free water ($\alpha \approx 0.06$; Payne, 1972), the average albedo is higher in the surfzone than in the relatively foam-free inner-shelf (Frouin et al., 1996). Deep-water albedo parameterizations have been developed for wind-generated whitecapping (e.g., Frouin et al., 1996; Jin et al., 2011; Koepke, 1984). However, surfzone foam is due to depth-limited wave breaking and does not require wind, making these parameterizations inappropriate for the surfzone. Recently, a surfzone albedo parameterization has been developed that uses offshore wave conditions, bathymetry, and a surfzone wave model (Sinnott & Feddersen, 2016).

The breaking wave-related surfzone albedo increase can be large (as much as 8× the inner-shelf albedo; Sinnott & Feddersen, 2016), and the subsequent decrease in solar radiation is significant. Thus, elevated surfzone albedo results in surfzone cooling relative to the inner-shelf. Similarly, the wave heating term can be a significant source of heat as including wave heating improved a surfzone heat budget (Sinnott & Feddersen, 2014). However, breaking wave albedo effects were not included, although a residual net surfzone cooling

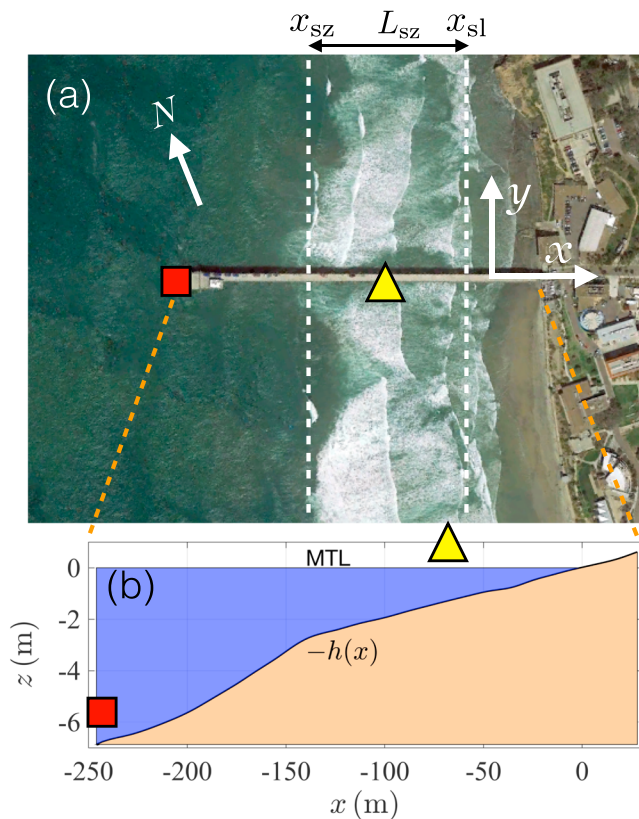


Figure 1. (a) Google earth image of the Scripps Institution of Oceanography pier experiment site near midtide with the x and y coordinates indicated. Locations of the wave and tide gauges (square) and radiometer (triangle) are shown relative to the pier. The surfzone width L_{sz} (white dotted) extends from the offshore limit of breaking x_{sz} to the effective shoreline x_{sl} where $h = 0.28$ m depth. (b) Cross-section along the Scripps Institution of Oceanography pier depicting MTL and mean bathymetry $z = -h(x)$ versus cross-shore coordinate x with wave gauge (square) and radiometer (triangle) locations indicated. The radiometer elevation above MTL is $z = 6.5$ m (not to scale in b). MTL = mean tide level.

was inferred. Thus, the relative importance of these two competing effects is unknown, as is how parameters such as wave height, beach slope, or latitude affect relative heating or cooling.

Here surfzone parameterizations of wave heating (Sinnott & Feddersen, 2014) and wave-induced albedo increase (Sinnott & Feddersen, 2016) are applied to yearlong observations quantifying the competing wave heating and albedo effects on surfzone heat fluxes. The experiment and analysis methods are detailed in section 2. Results quantifying the competing effects of wave heating and albedo-induced solar heating reduction are described in section 3. The implications of these competing effects for different parameter space (wave height, beach slope, latitude) is discussed in section 4.1. These competing wave-related heating and cooling effects are discussed relative to a previous heat budget at the same location (Sinnott & Feddersen, 2014) in section 4.2. Section 5 is a summary.

2. Methods

2.1. Instrumentation and Data Processing

A yearlong study was conducted at the Scripps Institution of Oceanography (SIO) pier (La Jolla California, 32.867N, 117.257W) between 25 October 2014 and 25 October 2015. The SIO pier extends 322 m west-north-west (288°) from Scripps beach into water depth $h \approx 7$ m (Figure 1a). The roughly alongshore uniform shoreline extends 200 m north to 500 m south of the pier. Cross-shore bathymetry profiles were conducted along the pier at 0.5 to 1 month intervals as wave conditions allowed. The cross-shore profile slopes gently with yearly bathymetric changes less than 0.3 m at any location, causing slope variation of less than 5%. The average slope in depths $h < 3.5$ m (typically includes the surfzone) is $s \approx 0.023$ (Figure 1b). A pier-end NOAA station (9410230) measured 6-min averaged tidal elevation η relative to the mean tide level. The cross-shore x coordinate is positive onshore, with the mean shoreline ($x = 0$) where mean tide level intersects the mean bathymetry. The alongshore coordinate y is positive toward the north, with $y = 0$ at the northern edge of the pier.

For the 365 days beginning 25 October 2014, hourly significant wave height H_s (zeroth moment of the hourly energy spectrum) and peak period T_p (period of the highest spectral energy density) were observed at the pier-end (square, Figures 1a and 1b) by the Coastal Data Information Program station 073 pier-mounted Paros pressure sensor. When the sensor was inoperative ($<7\%$ of the time), a spectral refraction wave model with very high skill and initialized from offshore buoys was used (O'Reilly & Guza, 1991, 1998; O'Reilly et al., 2016).

Concurrently, a Campbell Scientific NR01 four-way radiometer located midpier (triangle, Figures 1a and 1b) recorded 1-min averaged downwelling Q_{sw}^d and reflected upwelling Q_{sw}^u solar shortwave radiation (wavelengths 300 to 2800 nm) as described in Sinnott and Feddersen (2016). Although the radiometer was cleaned at regular intervals, rain or very dense fog caused water to accumulate on the glass optics. Additionally, rarely occurring extremely low tides moved the shoreline seaward of the radiometer location so that the sensors viewed sand rather than water. Data during these times were flagged and removed from the record (6% of all data). For this study, radiation data were hourly averaged onto the same temporal grid as the wave observations. These wave and radiation data were used to calibrate a parameterization relating offshore wave energy to surfzone albedo as described in section 2.2.3 and detailed in Sinnott and Feddersen (2016).

2.2. Analysis

2.2.1. Wave Model

The cross-shore transformation of normally incident narrow-banded waves on alongshore uniform beaches is described by one-dimensional wave and roller transformation models (e.g., Battjes & Stive, 1985; Ruessink

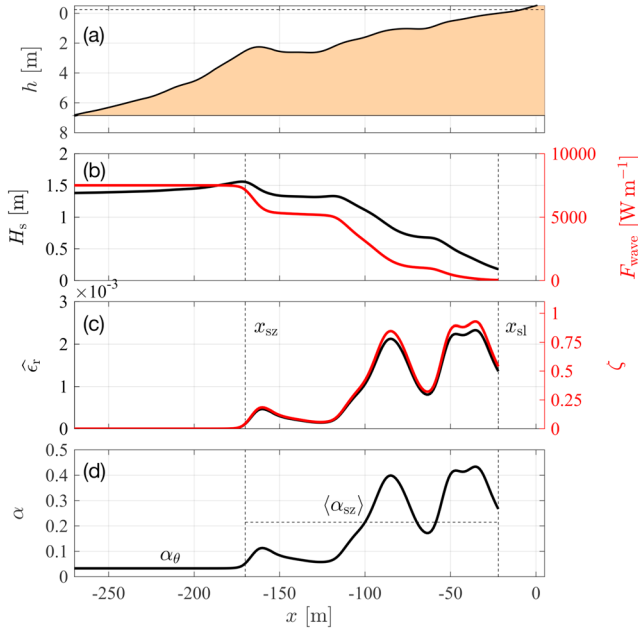


Figure 2. Example cross-shore (x) hourly averaged parameters from 5 May 2015 at 14:00 local time. (a) Bathymetry $h(x)$ (solid) and mean water level η (dotted), (b) significant wave height H_s (black) and associated cross-shore wave energy flux F_{wave} from (3) (red), (c) nondimensionalized roller energy dissipation $\hat{\epsilon}_r$ from (12) and foam fraction ζ from (13) as black and red, respectively, and (d) albedo on the inner-shelf α_θ and in the surfzone α_{sz} (14). The offshore breaking location $x_{sz} = -170$ m and effective shoreline $x_{sl} = -22$ m (black dashed in b, c, and d). The cross-shore averaged surfzone albedo $\langle \alpha_{sz} \rangle = 0.21$ (black dashed) and albedo where waves are not breaking (with clear sky conditions) $\alpha_\theta = 0.04$ are indicated in (d).

An example cross-shore wave transformation over bathymetry is illustrated (e.g.) on 5 May 2015 at 14:00 PDT (Figure 2a). Observed offshore wave height $H_s = 1.4$ m slightly increases onshore before breaking (black, Figure 2b) due to the shallowing bathymetry. Wave set-up and set-down are ignored in the transformation model as these adjustments contribute to a negligibly small variation in shoreline location. As waves break, H_s decreases from the outer surfzone to the shoreline, also reducing the wave energy flux F_{wave} (red, Figure 2b).

The outer surfzone boundary, x_{sz} (vertical dotted in Figures 2b–2d), is defined as where breaking wave dissipation is nonnegligible and corresponds to the maximum in H_s . Wave transformation models are not designed for shallow swash zones. Thus, an *effective shoreline*, x_{sl} , is defined as the first offshore location where $h > 0.28$ m, where the wave roller model is still applicable. Waves in water shallower than $h = 0.28$ m are considered swash and this region is ignored. The effective surfzone width L_{sz} is

$$L_{sz} = x_{sl} - x_{sz} \quad [\text{m}]. \quad (6)$$

For the example in Figure 2, $x_{sz} = -170$ m and $x_{sl} = -22$ m, making the effective surfzone width $L_{sz} = 148$ m.

2.2.2. Wave Heating

Cross-shore wave energy flux is dissipated across the surfzone by breaking (1). Since wave reflection on shallow sloping beaches is small (Elgar et al., 1994) as is export of mechanical energy from the surfzone (Sinnott & Feddersen, 2014), the bulk of the wave energy flux is frictionally dissipated inside the surfzone, eventually as heat. Note that the wave heating estimate here is an upper bound. Assuming the surfzone is well mixed, the heating from wave energy flux dissipation occurs over the entire surfzone width. Thus, the cross-surfzone averaged additional heat flux (relative to no wave breaking on the inner-shelf) due to the dissipation of breaking waves is

$$Q_{\text{wave}} = \frac{F_{\text{wave}}^{(x_{sz})} - F_{\text{wave}}^{(x_{sl})}}{L_{sz}} \quad [\text{W}/\text{m}^2], \quad (7)$$

et al., 2001; Thornton & Guza, 1983). The wave transformation is given by

$$\frac{d}{dx}(Ec_g) = -\epsilon_b, \quad (1)$$

where E is the wave energy density, c_g is the linear group velocity given by peak period and depth, and ϵ_b is the bulk breaking wave dissipation. The wave energy density is

$$E = \frac{1}{16} \rho g H_s^2, \quad (2)$$

where ρ is water density, g is gravity, and H_s is the significant wave height. The cross-shore wave energy flux at location x is

$$F_{\text{wave}}^{(x)} = Ec_g \quad [\text{W}/\text{m}]. \quad (3)$$

The model adapted here follows Church and Thornton (1993) with standard breaking parameters ($B = 0.9$ and $\gamma = 0.57$).

Similarly, the wave roller transformation describes the dissipation along a breaking wave face with energy equation (e.g., Ruessink et al., 2001)

$$\frac{d}{dx}(2E_r c) = -\epsilon_r + \epsilon_b. \quad (4)$$

Here E_r is the roller energy density, c is the linear phase speed, and roller dissipation ϵ_r (analogous to foam) is

$$\epsilon_r = \frac{2gE_r \sin \beta}{c}, \quad (5)$$

with wave slope $\beta = 0.1$ (e.g., Deigaard, 1993; Walstra et al., 1996). The model boundary conditions are the pier-end yearlong hourly H_s and peak period observations.

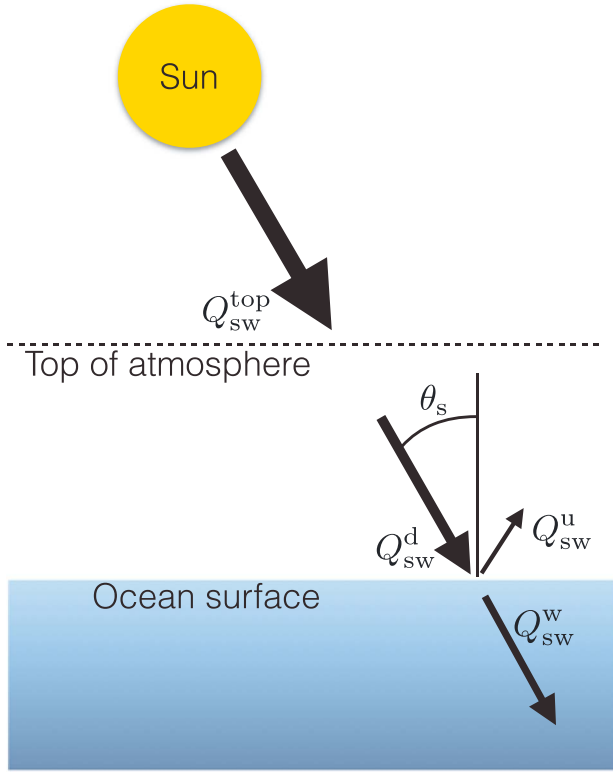


Figure 3. Schematic depicting the shortwave solar radiation (Q_{SW} , arrows) at different locations: the top of the atmosphere (dotted line) Q_{SW}^{top} , downwelling to the ocean surface Q_{SW}^d , water-entering Q_{SW}^w , and upwelling (reflected) Q_{SW}^u from the ocean surface. The solar zenith angle is θ_s .

where superscripts indicate the cross-shore flux location. This term Q_{wave} is denoted wave heating. In the example, at x_{sz} , $F_{wave}^{(x_{sz})} = 7,500$ W/m but at x_{sl} , $F_{wave}^{(x_{sl})} = 33$ W/m (red, Figure 2b), implying that at this example time, there is a 7,467 W/m energy flux convergence in the surfzone (or ≈ 50 W/m²) which is largely viscously dissipated and converted to heat. Over the year, hourly Q_{wave} is estimated from observed H_s through (7) and (3).

2.2.3. Solar Radiation

Top of the atmosphere shortwave solar radiation (Q_{SW}^{top} in Figure 3) is

$$Q_{SW}^{top} = S \cos(\theta_s) \Gamma^{-2} \quad [\text{W/m}^2], \quad (8)$$

where S is the solar constant, θ_s is the solar zenith angle (sun declination angle from vertical) which varies on diurnal and seasonal time scales, and Γ is the ratio of the actual to mean earth-sun separation distance, which varies annually (e.g., Whiteman & Allwine, 1986). Atmospheric attenuation and clouds reduce Q_{SW}^{top} so that the downwelling radiation at the ocean surface is $Q_{SW}^d < Q_{SW}^{top}$ (Figure 3). The atmospheric reduction in downwelling shortwave solar radiation is defined as

$$\Delta Q_{SW}^d = Q_{SW}^{top} - Q_{SW}^d \quad [\text{W/m}^2], \quad (9)$$

and indicates atmospheric optical depth or cloudiness. The shortwave albedo (reflectance) is the ratio of the total reflected (upward) solar radiation to the downwelling solar radiation at the ocean surface,

$$\alpha = \frac{Q_{SW}^u}{Q_{SW}^d}, \quad (10)$$

so that the water-entering shortwave radiation (Figure 3) is

$$Q_{SW}^w = Q_{SW}^d (1 - \alpha) \quad [\text{W/m}^2]. \quad (11)$$

Thus, changes to either the available downwelling radiation Q_{SW}^d or the albedo α affect the water-entering shortwave radiation and thus solar heating.

2.2.4. Inner-Shelf and Surfzone Albedo

In direct sunlight, standard nonwave breaking albedo parameterizations depend only on solar zenith angle θ_s (Briegleb et al., 1986; Payne, 1972; Taylor et al., 1996). In diffuse light (defined here when the ratio of atmospheric reduction in shortwave radiation to top-of-atmosphere shortwave radiation $\Delta Q_{SW}^d / Q_{SW}^{top} > 0.5$), ocean surface albedo is near 0.06 and no longer depends on θ_s (Payne, 1972). Thus, here the inner-shelf albedo (where waves are not breaking) α_θ is defined following Taylor et al. (1996) with specular reflection for $\Delta Q_{SW}^d / Q_{SW}^{top} \leq 0.5$ (direct sunlight). In diffuse light ($\Delta Q_{SW}^d / Q_{SW}^{top} > 0.5$) $\alpha \approx 0.06$ (Payne, 1972). Latitude and local time define θ_s following Reda and Andreas (2008). This θ_s dependent parameterization works well for inner-shelf observations at this site (Sinnott & Feddersen, 2016),

Surfzone albedo is parameterized following Sinnott and Feddersen (2016). The foam fraction ζ is a function of the nondimensionalized wave roller dissipation $\hat{\epsilon}_r$,

$$\hat{\epsilon}_r = \frac{\epsilon_r}{\rho(gh)^{3/2}}, \quad (12)$$

where nondimensionalization is denoted with ($\hat{\cdot}$). The example cross-shore $\hat{\epsilon}_r$ profile (black, Figure 2c) has peaks where waves are breaking over shallowing bathymetry and troughs where bathymetry is flatter or wave height is very low. Over the range of $\hat{\epsilon}_r$ typically observed at this location, the foam fraction ζ and $\hat{\epsilon}_r$ are linearly related (Sinnott & Feddersen, 2016) so that

$$\zeta(x) = m \hat{\epsilon}_r(x), \quad (13)$$

where $m = 398$ is a constant best-fit parameter. The example cross-shore ζ profile (red, Figure 2c) includes locations near $x = -75$ m and $x = -40$ m that are nearly continuously covered in foam, while only a few (large)

waves break seaward of $x = -150$ m reducing ζ . Under extremely energetic wave conditions, parts of the surfzone can saturate so that the fit produces $\zeta > 1$. When this occurs (less than 4% of the time) the foam fraction is restricted to the physical maximum $\zeta = 1$.

The wave affected (surfzone) albedo α_{sz} has contributions from both the foam-covered and foam-free surface, making

$$\alpha_{sz}(x) = \zeta(x)\alpha_f + (1 - \zeta(x))\alpha_\theta, \quad (14)$$

(Figure 2d). Here the best-fit $\alpha_f = 0.465$ (Sinnett & Feddersen, 2016) and α_θ is the θ_s parameterized albedo of foam-free water (Taylor et al., 1996). Onshore of the outer surfzone limit (x_{sz} , where waves begin to break) albedo increases above α_θ due to surface foam. Generally, albedo increases as the surfzone depth decreases, with variations caused by undulations in bathymetry. In the very shallow inner-surfzone, nearly all waves are breaking and the surfzone is nearly saturated in foam, so that $\alpha_{sz} \approx \alpha_f$.

The cross-shore surfzone average foam fraction is

$$\langle \zeta \rangle = \frac{1}{L_{sz}} \int_{x_{sl}}^{x_{sz}} \zeta dx, \quad (15)$$

which with (14) yields a cross-shore average surfzone albedo $\langle \alpha_{sz} \rangle$ (as in Figure 2d),

$$\langle \alpha_{sz} \rangle = \langle \zeta \rangle \alpha_f + (1 - \langle \zeta \rangle) \alpha_\theta. \quad (16)$$

Here $\langle \cdot \rangle$ indicates cross-shore averaging. From (11), the surfzone averaged albedo-induced solar heating reduction relative to the inner-shelf is then

$$\Delta Q_{sw}^w = Q_{sw}^d (\alpha_\theta - \langle \alpha_{sz} \rangle) \quad [W/m^2]. \quad (17)$$

Both the amount of available downwelling radiation Q_{sw}^d and the albedo difference between the surfzone and inner-shelf affect ΔQ_{sw}^w . As $\langle \alpha_{sz} \rangle > \alpha_\theta$, the surfzone has an albedo-induced cooling relative to the inner-shelf. Over the year, hourly ΔQ_{sw}^w is estimated with H_s and Q_{sw}^d via (17).

At this quartz-sand beach, this albedo parameterization does not explicitly consider the albedo of the seabed and suspended sediment, which can be important for other regions such as coral reefs (e.g., Hochberg et al., 2003) and estuaries (e.g., Fogarty et al., 2017). At small θ_s , the albedo of wet sand is about 0.07 (e.g., Dickinson, 1983), thus seabed reflections are weak. Furthermore, due to breaking wave-generated turbulence suspending sediment, the surfzone optical depth is typically small (e.g., Rippey, Franks, Feddersen, Guza, & Warrick, 2013) such that little light penetrates to the seabed. Surfzone suspended sediment concentrations above 5 g/L are unusual except near the seabed (e.g., Beach & Sternberg, 1996), and thus near-surface sand reflectance that contribute to albedo is also expected to be weak. Colocated instantaneous surfzone albedo and video observations clearly show that breaking wave foam drives albedo time-dependence, and when no waves are breaking, observed albedo agrees with the Taylor et al. (1996) parameterization (Sinnett & Feddersen, 2016).

3. Observations and Results

3.1. Observed Q_{sw}^d , H_s , F_{wave} , and Albedo

The top of the atmosphere Q_{sw}^{top} varies with θ_s and Γ on diurnal and seasonal time scales, so that the daily maximum Q_{sw}^{top} varies seasonally (red, Figure 4a). At the water surface available downwelling solar radiation Q_{sw}^d primarily varied diurnally, but also varied at synoptic to seasonal time scales (black, Figure 4a). On clear days, atmospheric attenuation resulted in $\Delta Q_{sw}^d / Q_{sw}^{top} \approx 0.25$. Clouds decreased the available Q_{sw}^d further (Figure 4b). In winter, cloudy periods usually lasted a few days (jagged peaks, Figure 4b) and were frequently accompanied by rain causing short Q_{sw}^d data gaps. In the very late spring and early summer, coastal fog persisted for longer periods causing $\Delta Q_{sw}^d / Q_{sw}^{top}$ to remain elevated (Figure 4b). Early spring, late summer, and early fall were typically less cloudy.

Pier-end significant wave height H_s typically varied synoptically between 0.5 and 1.5 m, with generally larger waves in winter and spring, and smaller waves in summer and fall (Figure 4c). Pier-end peak wave period was usually between 7 and 13 s (not shown). The mixed barotropic tide typically varied ± 1 m (not shown) inducing

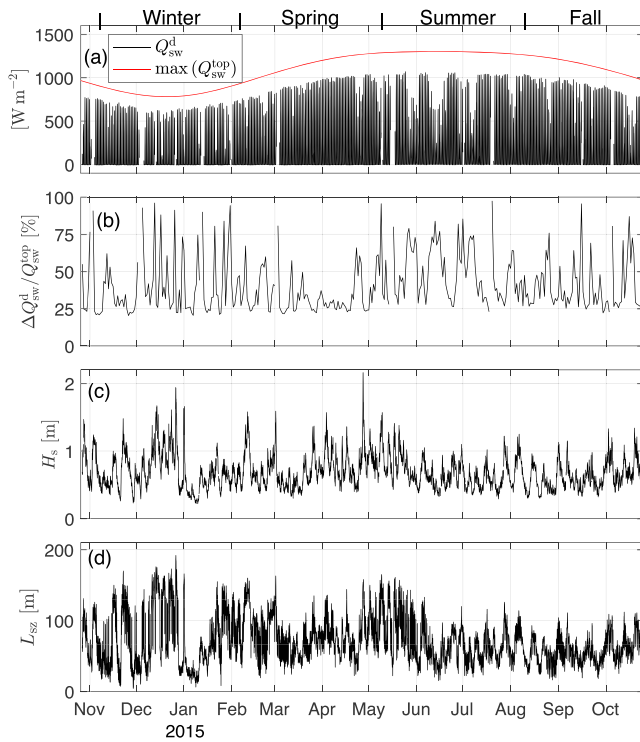


Figure 4. Yearlong time series of (a) daily maximum solar radiation at the top-of-atmosphere max Q_{sw}^{top} (red) and hourly averaged downwelling shortwave solar radiation to the ocean surface Q_{sw}^d (black), (b) daily percent reduction of downwelling solar shortwave radiation due to cloud cover $\Delta Q_{sw}^d/Q_{sw}^{top}$, (c) pier-end significant wave height H_s , and (d) surfzone width L_{sz} (6). Seasons denoted in (a) are 91 days long, centered on each solstice and equinox. Data in (a) are removed when rain obscured the radiometer.

ensemble averaged $\langle \alpha_{sz} \rangle$ elevated by 0.19 over α_θ . Wave, tide, and bathymetry variability influence $\langle \zeta \rangle$ and thus contribute to the relatively large $\langle \alpha_{sz} \rangle$ variability (red shaded).

3.2. Competing Wave Effects: ΔQ_{sw}^w and Q_{wave}

Breaking wave energy dissipation leads to surfzone wave heating Q_{wave} (7). Wave breaking also increases albedo, thereby reducing the water-entering shortwave solar radiation relative to the inner-shelf by an amount ΔQ_{sw}^w (17). Here these two competing effects are examined. Variability in Q_{wave} and ΔQ_{sw}^w occur on seasonal, synoptic, diurnal, and semidiurnal time scales through variation in H_s , θ_s , Q_{sw}^d , and L_{sz} . Here Q_{wave} and ΔQ_{sw}^w are daily (24 hr) averaged to examine their relative effects on synoptic and seasonal time scales.

Henceforth, all Q variables will be daily averaged.

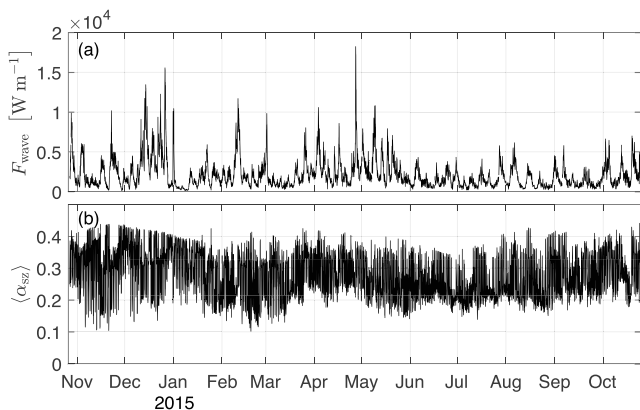


Figure 5. Hourly (a) pier-end wave energy flux F_{wave} (3) and (b) cross-shore averaged surfzone albedo $\langle \alpha_{sz} \rangle$ (16) versus time of year.

a roughly ± 43 m variation in x_{s1} . Wave and tide conditions, together with the evolving bathymetry, affected the surfzone width L_{sz} (Figure 4d). Average $L_{sz} = 84$ m, but was at times above 150 m during strong wave events and as small as 4 m when waves were small. Time periods were excluded from analysis when waves were very small and x_{sz} was in less than 0.5 m depth (*i.e.*, $L_{sz} < 10$, less than 0.2% of all data).

At the outer surfzone boundary, wave energy flux mean and standard deviation $F_{wave}^{(Q_{sz})} = 2,149 \pm 1,826$ W/m driven primarily by variable H_s through (3) on synoptic time scales (Figure 5a). Large wave events have an outsized contribution to F_{wave} due to the quadratic relationship between F_{wave} and H_s (3). Seasonal H_s variability generally elevated F_{wave} in wintertime and reduced F_{wave} in summertime. The cross-shore average surfzone albedo mean and standard deviation $\langle \alpha_{sz} \rangle = 0.28 \pm 0.07$ (Figure 5b) and was more than three times the mean inner-shelf albedo. Surfzone albedo $\langle \alpha_{sz} \rangle$ varied on tidal, diurnal, and seasonal time scales, and usually much more rapidly than F_{wave} .

The daylight variation of $\langle \alpha_{sz} \rangle$ and α_θ is examined with ensemble averages. Albedo estimates are removed when solar zenith angle is large ($|\theta_s| > 80^\circ$) to remove near-horizon effects. For each day, the daylight albedo estimates are normalized onto a standard 12 hr time-period removing seasonal daylight variations. These are subsequently binned over all the days in the year, allowing interday surfzone and inner-shelf albedo comparison. Daily ensemble averaged α_θ (blue line, Figure 6) has strong solar zenith angle θ_s dependence, with elevated albedo at low sun angles near sunrise and sunset. Seasonal variation in θ_s and cloud cover variation account for the relatively small α_θ deviation from the mean (blue shaded). As the surfzone has fractional foam coverage, $\langle \alpha_{sz} \rangle$ retains some θ_s dependence, although weaker than α_θ , with elevated $\langle \alpha_{sz} \rangle$ at larger $|\theta_s|$ (red line, Figure 6). However, surfzone foam elevates $\langle \alpha_{sz} \rangle$ above α_θ , with midday

Breaking wave-related heat flux contributions varied over the year (Figure 7) with Q_{wave} always increasing (positive) surfzone heat flux and ΔQ_{sw}^w always reducing (negative) surfzone heat flux relative to the inner-shelf. Over the year, the mean and standard deviation of the daily averaged $Q_{wave} = 28 \pm 11$ W/m² (red) and $\Delta Q_{sw}^w = -41 \pm 16$ W/m² (blue). Thus, at this location, the combined effect of Q_{wave} and ΔQ_{sw}^w typically reduced the surfzone heat flux relative to the inner-shelf. Both daily averaged Q_{wave} and ΔQ_{sw}^w varied on synoptic to seasonal time scales. However, daily averaged Q_{wave} and ΔQ_{sw}^w were uncorrelated ($r^2 = 0.04$) as Q_{wave} depends on incident H_s (Figure 4c) whereas ΔQ_{sw}^w depends also on clouds and Q_{sw}^{top} . Throughout most of summer, clouds reduced Q_{sw}^d and waves were small (Figures 4a–4c). Thus, the yearly maximum $|\Delta Q_{sw}^w|$ occurred in April when waves were larger and cloudiness lower, rather than at the summer solstice (21 June) when Q_{sw}^{top} is maximum.

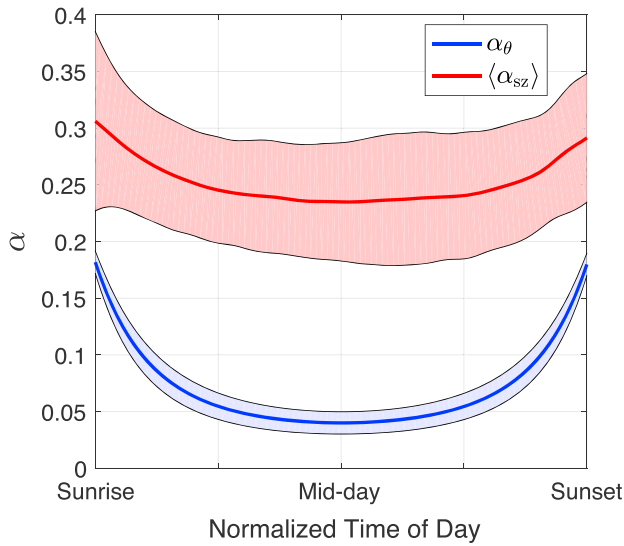


Figure 6. Daily ensemble averaged albedo with no wave breaking α_θ (blue) and daily ensemble averaged cross-shore averaged surfzone albedo $\langle \alpha_{sz} \rangle$ (red) versus normalized time of day. Shading is \pm one standard deviation from the mean.

The relative effects of Q_{wave} and ΔQ_{sw}^w have a seasonal dependence (Figure 8). In winter, $Q_{\text{sw}}^{\text{top}}$ is low and cloudiness $\Delta Q_{\text{sw}}^d/Q_{\text{sw}}^{\text{top}}$ can be high reducing $|\Delta Q_{\text{sw}}^w|$. Wintertime waves are also relatively large with $Q_{\text{wave}} > 40 \text{ W/m}^2$ about 20% of the time. The combined effect in winter heats the surfzone (to the right of the 1:1 line) relative to the inner-shelf 47% of the time (Figure 8a). In contrast, summertime waves were relatively small with $Q_{\text{wave}} > \text{W/m}^2$ only 5% of the time. The combined effect in summer cools the surfzone relative to the inner-shelf 96% of the time (Figure 8c).

Spring is characterized by a wide range of both Q_{wave} and ΔQ_{sw}^w (Figure 8b). Spring had few clouds, with $\Delta Q_{\text{sw}}^d/Q_{\text{sw}}^{\text{top}} > 40\%$ only a quarter of the time (compared to over half the time in summer). Spring also contained some of the largest H_s , resulting in the daily averaged $Q_{\text{wave}} > 50 \text{ W/m}^2$ 11% of the time. The fall ΔQ_{sw}^w distribution is slightly lower than in summer (Figure 8d). Fall $Q_{\text{sw}}^{\text{top}}$ is smaller than in summer (red, Figure 4a), yet fall skies were clearer (lower $\Delta Q_{\text{sw}}^d/Q_{\text{sw}}^{\text{top}}$) relative to summer such that mean Q_{sw}^d was reduced by only 5%. Occasional large wave events in late fall (more typical of winter conditions) widened the fall Q_{wave} distribution compared to summer. The seasonal variation in the Q_{wave} and ΔQ_{sw}^w relationship demonstrates the effect of parameters such as the incident H_s , cloudiness, and $Q_{\text{sw}}^{\text{top}}$.

3.3. Surfzone Adiabatic Temperature Change

As temperature is relevant to circulation dynamics, cross-shore exchange, and ecology, relating Q_{wave} and ΔQ_{sw}^w to an adiabatic temperature change is useful for understanding their relative effects. Relative to the inner-shelf, the daily averaged combined surfzone heat flux Q_{net} is

$$Q_{\text{net}} = Q_{\text{wave}} + \Delta Q_{\text{sw}}^w \quad [\text{W/m}^2],$$

with positive Q_{net} implying surfzone warming relative to the inner-shelf. For a planar beach slope, the surfzone daily adiabatic temperature change ΔT induced by Q_{net} is

$$\Delta T = \frac{t_{\text{day}} Q_{\text{net}}}{1/2 h_{\text{sz}} \rho c_p} \quad [^\circ\text{C}], \quad (18)$$

where $t_{\text{day}} = 86,400 \text{ s}$ is the duration of a day and h_{sz} is the outer surfzone boundary depth. Here the surfzone is assumed adiabatic (insulated) with no other breaking wave-induced heat fluxes (e.g., surfzone to inner-shelf exchange or air-sea fluxes).

Over the year, the daily adiabatic ΔT (18) was negative 75% of the time (black dots, Figure 9), with a mean and standard deviation of $\Delta T = -0.5 \pm 0.6 \text{ }^\circ\text{C}$. The 30-day ΔT mean and standard deviation also varied seasonally (red dots and red lines, Figure 9). Wintertime mean and standard deviation $\Delta T = 0.0 \pm 0.4 \text{ }^\circ\text{C}$ as wintertime Q_{net} is near zero. Beginning in early spring, ΔT typically becomes negative, with mean and standard deviation $\Delta T = -0.7 \pm 0.5 \text{ }^\circ\text{C}$ between March and September. In late summer and early fall with low clouds and small waves, ΔT can be as low as $-1.9 \text{ }^\circ\text{C}$. Daily ΔT variability was largest in spring and late summer when $Q_{\text{sw}}^{\text{top}}$ was high, but intermittent clouds or coastal fog caused large changes in ΔQ_{sw}^d . The late fall $Q_{\text{sw}}^{\text{top}}$ reduction and overall H_s increase (Figures 4a and 4c) prompted a return to winter conditions. In the adiabatic limit, net surfzone heat flux changes induced by Q_{wave} and ΔQ_{sw}^w are substantial and can induce significant ($\mathcal{O}(1 \text{ }^\circ\text{C})$) temperature changes.

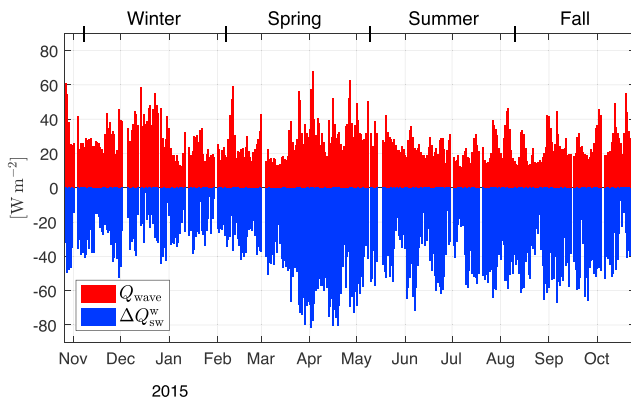


Figure 7. Yearlong time series of daily (24 hr) averaged wave heating Q_{wave} (7) and albedo-induced solar heating reduction ΔQ_{sw}^w (17) as indicated in the legend.

4. Discussion

4.1. Scaling for an Idealized Surfzone

Parameters affecting surfzone averaged ΔQ_{sw}^w and Q_{wave} are explored with scalings for a constant slope surfzone, lending insight to potential application at other sites with variable $Q_{\text{sw}}^{\text{top}}$, clouds, incident waves, and beach

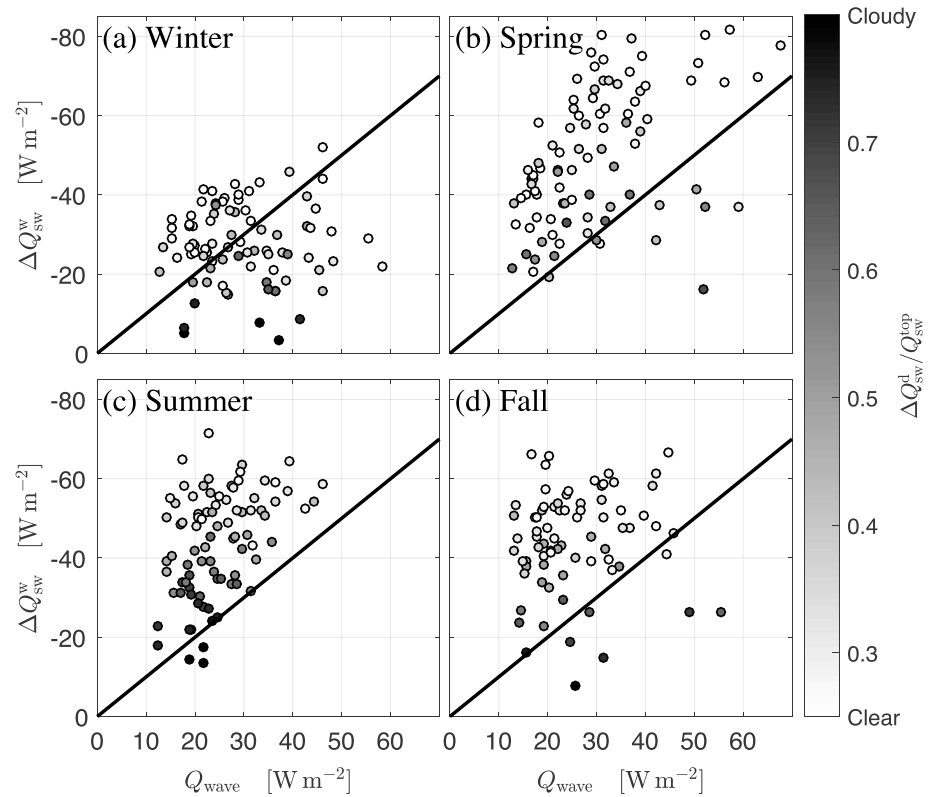


Figure 8. Daily averaged albedo-induced solar heating reduction ΔQ_{sw}^w versus the daily averaged wave heating Q_{wave} for each season. Symbols are shaded according to $\Delta Q_{sw}^d / Q_{sw}^{top}$ representing bulk cloudiness (Figure 4b). Daily averaged values fall to the right or left of the 1:1 line (solid black) contributing to net heat flux increase or decrease, respectively, relative to the inner-shelf.

slope. Although ΔQ_{sw}^w and Q_{wave} are uncorrelated, both depend on incident wave conditions, so a relationship exists between the two with added variability from the other nonwave factors such as bathymetric slope s and downwelling solar radiation at the water surface Q_{sw}^d . For an idealized surfzone of constant bathymetric slope s and constant γ , the surfzone averaged foam fraction $\langle \zeta \rangle$ (15) can be related to the nondimensionalized roller dissipation through (13) by surfzone averaging both the numerator and denominator in (12). The surfzone averaged $\hat{\epsilon}_r$ is simply $Q_{wave} = F_{wave} / L_{sz}$, and for a planar slope the representative (surfzone averaged)

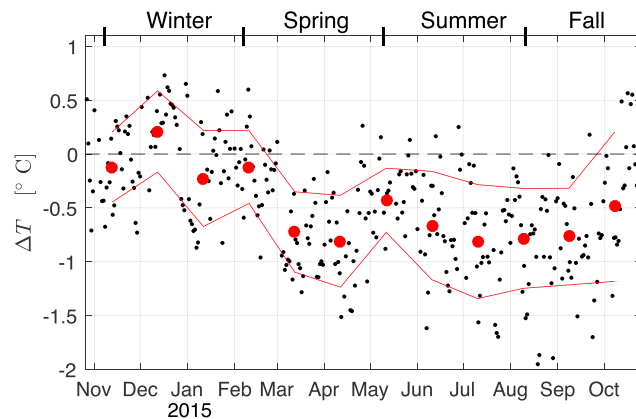


Figure 9. Yearly time series of daily adiabatic surfzone temperature change ΔT (black dots) as in (18) due to the competing wave effects of wave heating Q_{wave} and albedo-induced solar heating reduction ΔQ_{sw}^w . 30-day averages (red dots) and \pm standard deviation (red lines), along with the $\Delta T = 0$ (dashed black), are highlighted for reference.

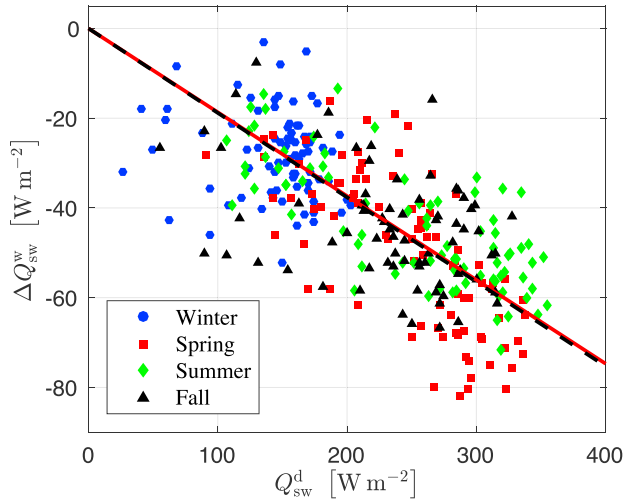


Figure 10. Daily averaged albedo-induced solar heating reduction ΔQ_{SW}^w (17) versus observed daily averaged downwelling solar radiation Q_{SW}^d . Symbols are identified (color and shape) by season. The best-fit slope of -0.19 (red line) deviates less than 1% from the idealized slope (dashed black line) from (21). The squared correlation $r^2 = 0.48$.

$h^{3/2}$ becomes $(2/5)h_{sz}^{3/2}$. Thus, bulk surfzone nondimensional roller dissipation $\hat{\epsilon}_r$ can be scaled as

$$\hat{\epsilon}_r = \frac{Q_{wave}}{\frac{2}{5} \rho (g h_{sz})^{3/2}}, \quad (19)$$

where the outer surfzone boundary depth $h_{sz} = H_{sb}/\gamma$, H_{sb} is the significant wave height at breaking, and $\gamma = 0.57$ is the breaking parameter. The surfzone averaged foam fraction $\langle \zeta \rangle$ is found applying (18) to (13) so that

$$\langle \zeta \rangle = \frac{m Q_{wave}}{\frac{2}{5} \rho (g h_{sz})^{3/2}} = \frac{5}{32} m s \gamma^2, \quad (20)$$

where $m = 398$. The surfzone averaged $\langle \zeta \rangle$ is independent of H_s , yet is linearly related to bathymetric slope s . Thus, the ratio of daily averaged ΔQ_{SW}^w and Q_{SW}^d is expected to be

$$\frac{\Delta Q_{SW}^w}{Q_{SW}^d} = \langle \zeta \rangle (\bar{\alpha}_\theta - \alpha_f) = \frac{5}{32} m s \gamma^2 (\bar{\alpha}_\theta - \alpha_f), \quad (21)$$

where $\bar{\alpha}_\theta$ is the constant daily averaged albedo of the inner-shelf. For constant s and γ and daily averaged $\bar{\alpha}_\theta$, the daily averaged ΔQ_{SW}^w and Q_{SW}^d is expected to be linearly related.

The linear relationship between daily averaged ΔQ_{SW}^w and Q_{SW}^d (Figure 10, has squared correlation $r^2 = 0.48$ ($p < 0.01$)) with best-fit slope -0.19 (red line). This implies that the daily averaged surfzone albedo is on average 0.19 larger than the inner-shelf. With an idealized (constant) bathymetric slope $s = 0.023$, daily averaged clear-sky inner-shelf albedo $\bar{\alpha}_\theta = 0.06$ (e.g., Payne, 1972), and foam albedo $\alpha_f = 0.465$ as in section 2.2.4, the surfzone averaged foam fraction (20) applied to (21) yields a theoretical slope $\langle \zeta \rangle (\bar{\alpha}_\theta - \alpha_f) = -0.19$ (dashed black line, Figure 10) which is less than 1% different from the best-fit slope to observations. Deviations from the scaling (21) are potentially due to tidal and incident H_s variation together with the realistic and variable nonplanar bathymetry. The linear relationship correlation between ΔQ_{SW}^w and Q_{SW}^d (Figure 10) that matches the scaling (21) demonstrate the suitability of (20) and (21) to effectively scale ΔQ_{SW}^w on gently sloping and alongshore uniform beaches.

Next, for a planar slope using (21), the ratio of surfzone daily averaged ΔQ_{SW}^w magnitude to Q_{wave} is

$$\frac{|\Delta Q_{SW}^w|}{Q_{wave}} = \left[\left| \frac{5 m \gamma^{3/2} (\bar{\alpha}_\theta - \alpha_f)}{2 \rho g^{3/2}} \right| \right] \frac{Q_{SW}^d}{H_{sb}^{3/2}}, \quad (22)$$

where the bracketed quantity is a constant and is independent of bathymetric slope. Thus, the ratio $|\Delta Q_{SW}^w|/Q_{wave}$ largely depends on $Q_{SW}^d/H_{sb}^{3/2}$. The downwelling solar radiation Q_{SW}^d depends on cloudiness and top of the atmosphere Q_{SW}^{top} . Daily averaged Q_{SW}^d is found from (8), and cloudiness (atmospheric attenuation or optical depth) may be estimated from terrestrial or satellite products (e.g., CERES, 2018). The wave height at the breakpoint H_{sb} can be well modeled (e.g., Ruessink et al., 2003) given incident wave conditions.

The $|\Delta Q_{SW}^w|/Q_{wave}$ scaling for an idealized surfzone (22) is compared with observations (Figure 11), illustrating how clouds, Q_{SW}^{top} , and H_{sb} affect the $|\Delta Q_{SW}^w|/Q_{wave}$ ratio. The observed $|\Delta Q_{SW}^w|/Q_{wave}$ ratio is largest for small H_{sb} and decreases for larger H_{sb} consistent with the scaling. For $H_{sb} > 1.5$ m, the observations and scaling have $|\Delta Q_{SW}^w|/Q_{wave} < 1$ (relative heating) at this location. For a clear sky (no clouds or constant atmospheric attenuation), Q_{SW}^d in (22) depends only on Q_{SW}^{top} , varying only by season and latitude. At a latitude of $33^\circ N$ (near the SIO pier) for the clear-sky summer solar maximum, the $|\Delta Q_{SW}^w|/Q_{wave}$ scaling (22) bounds the upper limit on the observed $|\Delta Q_{SW}^w|/Q_{wave}$ for a particular H_{sb} (Figure 11, solid black). For the $33^\circ N$ clear-sky winter solar minimum, the $|\Delta Q_{SW}^w|/Q_{wave}$ scaling intersects the observations (Figure 11, black dashed). Without clouds, $|\Delta Q_{SW}^w|/Q_{wave}$ observations are expected to fall between the black solid and dashed curves. However, the presence of clouds lower the observed Q_{SW}^d (and subsequently the $|\Delta Q_{SW}^w|/Q_{wave}$) for a particular H_{sb} . Thus, the scaling (22) sets an upper bound.

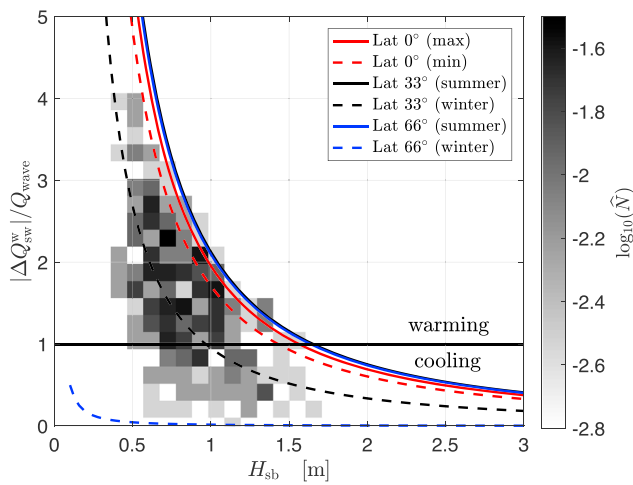


Figure 11. Normalized joint PDF (gray shaded) of daily averaged $|\Delta Q_{SW}^w|/Q_{wave}$ and significant wave height at breaking H_{sb} . The $|\Delta Q_{SW}^w|/Q_{wave} = 1$ line is highlighted, delineating relative cooling (> 1) and heating (< 1). Daily averaged $|\Delta Q_{SW}^w|/Q_{wave}$ observations at various For clear skies (25% atmospheric attenuation), the $|\Delta Q_{SW}^w|/Q_{wave}$ ratio versus H_{sb} is found from (22) and plotted for the summer (solar maximum, solid) and winter (solar maximum, dotted) at the equator ($0^\circ N$), 33° and 66° latitude (colored). Summer (solid) 33° and 66° latitude (black and blue) curves are nearly on top of each other.

The scaling for $|\Delta Q_{SW}^w|/Q_{wave}$ (22) can be used to estimate the relative importance of ΔQ_{SW}^w to Q_{wave} at other locations with variable latitude and seasonal top of the atmosphere Q_{SW}^{top} , cloud, beach slope, and wave conditions. At the equator ($0^\circ N$) seasonal variation in Q_{SW}^{top} is very small, resulting in a similar clear-sky $|\Delta Q_{SW}^w|/Q_{wave}$ and H_{sb} relationship year-round (red solid and dashed curves in Figure 11). At high latitudes, the seasonal difference in Q_{SW}^{top} is large, expanding the summer to winter difference. At $66^\circ N$, the summer clear-sky $|\Delta Q_{SW}^w|/Q_{wave}$ to H_{sb} relationship (Figure 11, blue solid) is nearly the same as at $33^\circ N$ (the experiment site). However, for wintertime clear skies, $|\Delta Q_{SW}^w|/Q_{wave} \ll 1$ for any $H_{sb} > 0.4$ m (Figure 11, blue dashed) indicating wave heating nearly always dominates at any beach exposed to the open ocean (not iced in). In contrast at $33^\circ N$, wintertime clear-sky $|\Delta Q_{SW}^w|/Q_{wave} < 1$ only for $H_{sb} > 1$ m. These significant latitude and seasonal differences in clear-sky $|\Delta Q_{SW}^w|/Q_{wave}$ will have implications for surfzone heat budgets from equator to Arctic. Note that carbonate sands or coral reef surfzones, which often have high optical clarity, may have additional albedo affects due to seabed reflections (e.g., Hochberg et al., 2003).

4.2. Wave heating Q_{wave} and Albedo-Induced Solar Radiation Reduction ΔQ_{SW}^w in Context

At the La Jolla, CA, experiment site, the parameters H_s , $h(x)$, Q_{SW}^d , Q_{SW}^{top} , and cloudiness ($\Delta Q_{SW}^d/Q_{SW}^{top}$) contribute to the breaking wave-induced positive or negative surfzone heat flux relative to the inner-shelf. Here the two terms Q_{wave} and ΔQ_{SW}^w are placed in the context of a previous surfzone heat

budget. Including wave heating (Q_{wave}) but not ΔQ_{SW}^w improved a summertime binned mean surfzone heat budget on diurnal and longer time scales (Sinnott & Feddersen, 2014). However, here the summertime $|\Delta Q_{SW}^w|$ was usually greater than $|Q_{wave}|$ (Figure 8c). However, Q_{wave} and ΔQ_{SW}^w are uncorrelated ($r^2 < 0.04$). Thus, including Q_{wave} but not ΔQ_{SW}^w still improved the binned mean heat budget slope by reducing the unexplained variance. Sinnott and Feddersen (2014) also inferred a net surfzone cooling of $\approx 5,200$ W/m (or ≈ 90 W/m² over the average L_{sz} for the same period) required to balance the surfzone heat budget. Here the summer-averaged $\Delta Q_{SW}^w = 44$ W/m² (compare to the yearly averaged $\Delta Q_{SW}^w = 41$ W/m²) may account for nearly half the Sinnott and Feddersen (2014) inferred required net cooling. Advective processes, such as transient rip currents (e.g., Hally-Rosendahl et al., 2015) or nonlinear internal wave run up (e.g., Sinnott et al., 2018) may also contribute to the required relative surfzone cooling.

Breaking wave-induced changes to the surfzone latent or sensible heat flux are also modified by wave breaking due to surfzone spray and aerosol generation, which may also contribute to the surfzone heat budget. Parameterized (COARE) surfzone sensible heat flux estimations required an additional spray contribution when compared to surfzone covariance measurements (MacMahan et al., 2018). For the average wave dissipation observed at this site, the additional sensible heat flux due to breaking wave spray is ≈ 5 W/m², relatively small compared to Q_{wave} and ΔQ_{SW}^w at Scripps Beach. Spray droplets produced by breaking are typically large (Andreas, 2016) and quickly fall back to the surface before exchanging latent heat (MacMahan et al., 2018; Veron, 2015). However, the enthalpy exchange coefficient may be larger for a foamy sea surface than a foam-free surface (Chickadel, 2018), potentially enhancing surfzone latent heat flux. Examination of all surfzone heat flux terms is warranted to properly understand all the ways that breaking waves can affect the surfzone heat budget.

5. Summary

Nearshore heat and solar radiation budgets typically overlook breaking wave effects, and the relative importance of this adjustment is unknown. Here the relative effects of wave heating due to viscous dissipation of breaking waves Q_{wave} and albedo-induced solar heating reduction relative to the inner-shelf are studied with yearlong observations at the SIO (La Jolla, CA) pier. Wave energy flux at the outer surfzone boundary $F_{wave}^{ksz} = 2,149 \pm 1,826$ W/m, which dissipated over L_{sz} yielding a daily averaged wave heating contribution $Q_{wave} = 28 \pm 11$ W/m². Breaking waves partially covered the surfzone in foam, increasing albedo on average

by a factor of 3 relative to the inner-shelf. The increased surfzone albedo subsequently created a solar heating reduction relative to the inner-shelf of $\Delta Q_{SW}^w = 41 \pm 16 \text{ W/m}^2$. Usually at this location, the net effect ($Q_{wave} + \Delta Q_{SW}^w$) together act to cool the surfzone relative to the inner-shelf. However, the combined (Q_{wave} and ΔQ_{SW}^w) effect had seasonal dependence, with a net heating roughly half the time in winter, but only 4% of the time in summer.

On a beach of constant slope, the average surfzone foam fraction can be scaled as a function of beach slope, resulting in a surfzone averaged albedo (α_{sz}) that is independent of H_s . At the experiment site, ΔQ_{SW}^w and Q_{SW}^d are linearly related and are in good agreement with the scaling. Scalings also are developed to the relative breaking wave surfzone heat flux contribution. The amount of additional surfzone cooling or heating relative to the inner-shelf is related to the ratio of Q_{SW}^d to $H_{sb}^{3/2}$ at the outer surfzone boundary. Clouds, Q_{SW}^{top} , and H_{sb} affect the $|\Delta Q_{SW}^w|/Q_{wave}$ ratio and thus the relative surfzone cooling or heating. This scaling can be applied at other locations to determine the relative heating or cooling effects of surfzone breaking waves.

Acknowledgments

This publication was prepared under NOAA Grant NA14OAR4170075/ECKMAN, California Sea Grant College Program Project R/HCME-26, through NOAA's National Sea Grant College Program, U.S. Dept. of Commerce. Additional support for this work was provided in part by ONR (N00014-15-1-2117) and NSF (OCE-1558695). The radiometer boom arm was designed and manufactured by B. Woodward, B. Boyd, K. Smith, and R. Grenzeback. Deployment was aided by C. McDonald, R. Walsh, S. Mumma, G. Boyd, L. Parry, and many San Diego lifeguards. Wave data from the Coastal Data Information Program (CDIP) were provided with assistance from W. O'Reilly and C. Olfe. Atmospheric conditions and tide data were from NOAA station 9410230 and Earth Networks. J. Norris, R. Clemesha, S. Giddings, A. Suanda, D. Grimes, G. Pawlak, K. Davis, and two anonymous reviewers provided helpful feedback. We sincerely thank these people and institutions. Data are available at iodlabs.ucsd.edu/falk/szheat

References

- Andreas, E. L. (2016). Sea spray generation at a rocky shoreline. *Journal of Applied Meteorology and Climatology*, 55(9), 2037–2052. <https://doi.org/10.1175/JAMC-D-15-0211.1>
- Austin, J. A. (1999). The role of the alongshore wind stress in the heat budget of the North Carolina inner shelf. *Journal of Geophysical Research*, 104(C8), 18187–18203. <https://doi.org/10.1029/1998JC900122>
- Austin, J. A., & Lentz, S. J. (1999). The relationship between synoptic weather systems and meteorological forcing on the North Carolina inner shelf. *Journal of Geophysical Research*, 104(C8), 18,159–18,185. <https://doi.org/10.1029/1999JC900016>
- Battjes, J. A., & Stive, M. J. F. (1985). Calibration and verification of a dissipation model for random breaking waves. *Journal of Geophysical Research*, 90(C5), 9159–9167. <https://doi.org/10.1029/JC090iC05p09159>
- Beach, R. A., & Sternberg, R. W. (1996). Suspended-sediment transport in the surf zone: Response to breaking waves. *Continental Shelf Research*, 16(15), 1989–2003.
- Beardsley, R. C., Dever, E. P., Lentz, S. J., & Dean, J. P. (1998). Surface heat flux variability over the Northern California shelf. *Journal of Geophysical Research*, 103(C10), 21553–21586. <https://doi.org/10.1029/98JC01458>
- Boehm, A. B. (2003). Model of microbial transport and inactivation in the surf zone and application to field measurements of total coliform in northern Orange County, California. *Environmental Science & Technology*, 37(24), 5511–5517. <https://doi.org/10.1021/es034321x>
- Boehm, A. B., Grant, S. B., Kim, J. H., McGee, C. D., Mowbray, S., Clark, C., et al. (2002). Decadal and shorter period variability of surfzone water quality at Huntington Beach, California. *Environmental Science and Technology*, 36, 3885–3892.
- Boehm, A. B., Lluch-Cota, D. B., Davis, K. A., Winant, C. D., & Monismith, S. G. (2004). Covariation of coastal water temperature and microbial pollution at interannual to tidal periods. *Geophysical Research Letters*, 31, L06309. <https://doi.org/10.1029/2003GL019122>
- Briegleb, B., Minnis, P., Ramanathan, V., & Harrison, E. (1986). Comparison of regional clear-sky albedos inferred from satellite observations and model computations. *Journal of Climate and Applied Meteorology*, 25, 214–226.
- Broitman, B., Blanchette, C., & Gaines, S. (2005). Recruitment of intertidal invertebrates and oceanographic variability at Santa Cruz Island, California. *Limnology and Oceanography*, 50(5), 1473–1479.
- CERES (2018). Clouds and the Earth's Radiant Energy System. <https://doi.org/ceres.larc.nasa.gov/index.php>
- Chickadel, C. (2018). Personal Comm, email interview.
- Church, J., & Thornton, E. (1993). Effects of breaking wave-induced turbulence within a longshore-current model. *Coastal Engineering*, 20(1-2), 1–28.
- Davis, K. A., Lentz, S. J., Pineda, J., Farrar, J. T., Starczak, V. R., & Churchill, J. H. (2011). Observations of the thermal environment on Red Sea platform reefs: A heat budget analysis. *Coral Reefs*, 30(1.S1), 25–36. <https://doi.org/10.1007/s00338-011-0740-8>
- Deigaard, R. (1993). A note on the three dimensional shear stress distribution in a surfzone. *Coastal Engineering*, 20, 157–171.
- Dickinson, R. E. (1983). Land surface processes and climate—Surface albedos and energy balance. In R. E. Dickinson (Ed.), *Theory of climate, advances in geophysics* (Vol. 25, pp. 305–353). New York, USA: Elsevier. [https://doi.org/10.1016/S0065-2687\(08\)60176-4](https://doi.org/10.1016/S0065-2687(08)60176-4)
- Elgar, S., Herbers, T., & Guza, R. T. (1994). Reflection of ocean surface gravity waves from a natural beach. *Journal of Physical Oceanography*, 24, 1503–1511.
- Etter, P. C., Howard, M. K., & Cochrane, J. D. (2004). Heat and freshwater budgets of the Texas-Louisiana shelf. *Journal of Geophysical Research*, 109, C02024. <https://doi.org/10.1029/2003JC001820>
- Fairall, C., Bradley, E., Hare, J., Grachev, A., & Edson, J. (2003). Bulk parameterization of air-sea fluxes: Updates and verification for the COARE algorithm. *Journal of Climate*, 16(4), 571–591.
- Fairall, C., Bradley, E., Rogers, D., Edson, J., & Young, G. (1996). Bulk parameterization of air-sea fluxes for tropical ocean-global atmosphere coupled-ocean atmosphere response experiment. *Journal of Geophysical Research*, 101(C2), 3747–3764.
- Feddersen, F., Guza, R. T., Elgar, S., & Herbers, T. H. C. (1998). Alongshore momentum balances in the nearshore. *Journal of Geophysical Research*, 103, 15667–15676.
- Fewings, M. R., & Lentz, S. J. (2011). Summertime cooling of the shallow continental shelf. *Journal of Geophysical Research*, 116, C07015. <https://doi.org/10.1029/2010JC006744>
- Fischer, S., & Thatje, S. (2008). Temperature-induced oviposition in the brachyuran crab *Cancer setosus* along a latitudinal cline: Aquaria experiments and analysis of field-data. *Journal of Experimental Marine Biology and Ecology*, 357(2), 157–164. <https://doi.org/10.1016/j.jembe.2008.01.007>
- Fogarty, M. C., Fewings, M. R., Paget, A. C., & Dierssen, H. M. (2017). The influence of a sandy substrate, seagrass, or highly turbid water on albedo and surface heat flux. *Journal of Geophysical Research: Oceans*, 123, 53–73. <https://doi.org/10.1002/2017JC013378>
- Frouin, R., Schwindling, M., & Deschamps, P.-Y. (1996). Spectral reflectance of sea foam in the visible and near-infrared: In situ measurements and remote sensing implications. *Journal of Geophysical Research*, 101(C6), 14361–14371. <https://doi.org/10.1029/96JC00629>
- Goodwin, K. D., McNay, M., Cao, Y., Ebentier, D., Madison, M., & Griffith, J. F. (2012). A multi-beach study of *Staphylococcus aureus*, MRSA, and enterococci in seawater and beach sand. *Water Research*, 46(13), 4195–4207. <https://doi.org/10.1016/j.watres.2012.04.001>
- Hally-Rosendahl, K., Feddersen, F., Clark, D. B., & Guza, R. T. (2015). Surfzone to inner-shelf exchange estimated from dye tracer balances. *Journal of Geophysical Research: Oceans*, 120, 6289–6308. <https://doi.org/10.1002/2015JC010844>

- Hally-Rosendahl, K., Feddersen, F., & Guza, R. T. (2014). Cross-shore tracer exchange between the surfzone and the inner-shelf. *Journal of Geophysical Research: Oceans*, *119*, 4367–4388. <https://doi.org/10.1002/2013jc009722>
- Hochberg, E. J., Atkinson, M. J., & Andréfouët, S. (2003). Spectral reflectance of coral reef bottom-types worldwide and implications for coral reef remote sensing. *Remote Sensing of Environment*, *85*(2), 159–173. [https://doi.org/https://doi.org/10.1016/S0034-4257\(02\)00201-8](https://doi.org/https://doi.org/10.1016/S0034-4257(02)00201-8)
- Jin, Z., Qiao, Y., Wang, Y., Fang, Y., & Yi, W. (2011). A new parameterization of spectral and broadband ocean surface albedo. *Optics Express*, *19*(27), 26,429–26,443.
- Kennedy, R. M. (1992). Sea surface dipole sound source dependence on wave-breaking variables. *The Journal of the Acoustical Society of America*, *91*(4), 1974–1982. <https://doi.org/10.1121/1.403681>
- Klusek, Z., & Lisimenka, A. (2013). Acoustic noise generation under plunging breaking waves. *Oceanologia*, *55*(4), 809–836. <https://doi.org/https://doi.org/10.5697/oc.55-4.809>
- Koepke, P. (1984). Effective reflectance of oceanic whitecaps. *Applied Optics*, *23*(11), 1816–1824.
- Kumar, N., & Feddersen, F. (2017). The effect of Stokes drift and transient rip currents on the inner shelf. Part II: With stratification. *Journal of Physical Oceanography*, *47*(1), 243–260. <https://doi.org/10.1175/JPO-D-16-0077.1>
- Lentz, S. J. (1987). A heat budget for the Northern California shelf during CODE 2. *Journal of Geophysical Research*, *92*(C13), 14,491–14,509. <https://doi.org/10.1029/JC092iC13p14491>
- MacMahan, J., Thornton, E., Kosciński, J., & Wang, Q. (2018). Field observations and modeling of surf zone sensible heat flux. *Journal of Applied Meteorology and Climatology*, *57*, 1371–1383. <https://doi.org/10.1175/JAMC-D-17-0228.1>
- O'Reilly, W., & Guza, R. (1991). Comparison of spectral refraction and refraction-diffraction wave models. *Journal of Waterway Port Coastal and Ocean Engineering-ASCE*, *117*(3), 199–215.
- O'Reilly, W., & Guza, R. (1998). Assimilating coastal wave observations in regional swell predictions. Part I: Inverse methods. *Journal of Physical Oceanography*, *28*(4), 679–691.
- O'Reilly, W., Olfe, C. B., Thomas, J., Seymour, R., & Guza, R. (2016). The California coastal wave monitoring and prediction system. *Coastal Engineering*, *116*, 118–132. <https://doi.org/https://doi.org/10.1016/j.coastaleng.2016.06.005>
- Omand, M. M., Feddersen, F., Franks, P. J. S., & Guza, R. T. (2012). Episodic vertical nutrient fluxes and nearshore phytoplankton blooms in Southern California. *Limnology and Oceanography*, *57*, 1673–1688. <https://doi.org/10.4319/lo.2012.57.6.1673>
- Payne, R. E. (1972). Albedo of the sea surface. *Journal of Atmospheric Sciences*, *29*, 959–970.
- Phillips, N. (2005). Growth of filter-feeding benthic invertebrates from a region with variable upwelling intensity. *Marine Ecology Progress Series*, *295*, 79–89. <https://doi.org/10.3354/meps295079>
- Reda, I., & Andreas, A. (2008). Solar position algorithm for solar radiation applications (revised) (Tech. rep.) Golden, CO: National Renewable Energy Laboratory.
- Rippy, M. A., Franks, P. J. S., Feddersen, F., Guza, R., & Moore, D. (2013). Factors controlling variability in nearshore fecal pollution: The effects of mortality. *Marine Pollution Bulletin*, *66*(1), 191–198. <https://doi.org/https://doi.org/10.1016/j.marpolbul.2012.09.003>
- Rippy, M. A., Franks, P. J. S., Feddersen, F., Guza, R. T., & Warrick, J. A. (2013). Beach nourishment impacts on bacteriological water quality and phytoplankton bloom dynamics. *Environmental Science & Technology*, *47*, 6146–6154. <https://doi.org/10.1021/es400572k>
- Ruessink, B. G., Miles, J. R., Feddersen, F., Guza, R. T., & Elgar, S. (2001). Modeling the alongshore current on barred beaches. *Journal of Geophysical Research*, *106*, 22451–22463.
- Ruessink, B., Walstra, D., & Southgate, H. (2003). Calibration and verification of a parametric wave model on barred beaches. *Coastal Engineering*, *48*(3), 139–149. [https://doi.org/https://doi.org/10.1016/S0378-3839\(03\)00023-1](https://doi.org/https://doi.org/10.1016/S0378-3839(03)00023-1)
- Shroyer, E. L., Moum, J. N., & Nash, J. D. (2010). Vertical heat flux and lateral mass transport in nonlinear internal waves. *Geophysical Research Letters*, *37*, L08601. <https://doi.org/10.1029/2010GL042715>
- Sinnett, G., & Feddersen, F. (2014). The surf zone heat budget: The effect of wave heating. *Geophysical Research Letters*, *41*, 7217–7226. <https://doi.org/10.1002/2014GL061398>
- Sinnett, G., & Feddersen, F. (2016). Observations and parameterizations of surfzone albedo. *Methods in Oceanography*, *17*, 319–334. <https://doi.org/10.1016/j.mio.2016.07.001>
- Sinnett, G., Feddersen, F., Lucas, A. J., Pawlak, G., & Terrill, E. (2018). Observations of nonlinear internal wave run-up to the surfzone. *Journal of Physical Oceanography*, *48*, 531–554. <https://doi.org/10.1175/JPO-D-17-0210.1>
- Sinton, L. W., Finlay, R. K., & Linch, F. A. (1999). Sunlight inactivation of fecal bacteriophages and bacteria in sewage-polluted seawater. *Applied and Environmental Microbiology*, *65*(8), 3605–3613.
- Sinton, L., Hall, C., Lynch, P., & Davies-Colley, R. (2002). Sunlight inactivation of fecal indicator bacteria and bacteriophages from waste stabilization pond effluent in fresh and saline waters. *Applied and Environmental Microbiology*, *68*(3), 1122–1131.
- Smith, J. A., & Largier, J. L. (1995). Observations of nearshore circulation: Rip currents. *Journal of Geophysical Research*, *100*(C6), 10,967–10,975. <https://doi.org/10.1029/95JC00751>
- Surbeck, C. Q. (2009). Factors influencing the challenges of modelling and treating fecal indicator bacteria in surface waters. *Ecology*, *90*(2), 399–403. <https://doi.org/10.1002/eco.98>
- Taylor, J., Edwards, J., Glew, M., Hignett, P., & Slingo, A. (1996). Studies with a flexible new radiation code. II: Comparisons with aircraft short-wave observations. *Quarterly Journal of the Royal Meteorological Society*, *122*, 839–861.
- Thornton, E. B., & Guza, R. T. (1983). Transformation of wave height distribution. *Journal of Geophysical Research*, *88*(C10), 5925–5938.
- Veron, F. (2015). Ocean spray. *Annual Review of Fluid Mechanics*, *47*(1), 507–538. <https://doi.org/10.1146/annurev-fluid-010814-014651>
- Walstra, D. J. R., Mocke, G. P., & Smit, F. (1996). Roller contributions as inferred from inverse modelling techniques. In *Coastal Engineering Proceedings*. Retrieved from <https://icce-ojs-tamu.tdl.org/icce/index.php/icce/article/view/5298>
- Whiteman, C., & Allwine, K. (1986). Extraterrestrial solar radiation on inclined surfaces. *Environmental Software*, *1*(3), 164–169. [https://doi.org/10.1016/0266-9838\(86\)90020-1](https://doi.org/10.1016/0266-9838(86)90020-1)
- Whitlock, C. H., Bartlett, D. S., & Gurganus, E. A. (1982). Sea foam reflectance and influence on optimum wavelength for remote sensing of ocean aerosols. *Geophysical Research Letters*, *9*(6), 719–722. <https://doi.org/10.1029/GL009i006p00719>
- Wilkin, J. L. (2006). The summertime heat budget and circulation of southeast New England shelf waters. *Journal of Physical Oceanography*, *36*(11), 1997–2011. <https://doi.org/10.1175/JPO2968.1>